



High-density ultrafine RuP₂ with strong catalyst-support interaction driven by dual-ligand and tungsten-oxygen sites for hydrogen evolution at 1 A cm⁻²

Ya-Nan Zhou^a, Fu-Li Wang^a, Jun Nan^{a,b}, Bin Dong^{a,*}, Hui-Ying Zhao^a, Feng-Ge Wang^a, Ning Yu^a, Ren-Ni Luan^a, Da-Peng Liu^a, Yong-Ming Chai^{a,*}

^a State Key Laboratory of Heavy Oil Processing, College of Science, China University of Petroleum (East China), Qingdao 266580, PR China

^b CNOOC Tianjin Chemical Research and Design Institute Co., Ltd, Tianjin 300131, PR China

ARTICLE INFO

Keywords:

Ultrafine RuP₂
Dual-ligand
Metal-oxygen sites
W doping
Hydrogen evolution

ABSTRACT

Ultrafine and high-density RuP₂ based on coordination chemistry and catalyst-support correlation shows potential for hydrogen evolution reaction (HER). Herein, the uniform and high-density W-doped ultra-small RuP₂ (W_{0.05}-RuP₂@C₃N₄-NC) are synthesized by incorporating oxygen-bridged [WO₄] tetrahedron into tetraacetic acid (EDTA)-melamino-formaldehyde (MF) ligands. EDTA-MF shows strong metal-support interaction, dedicating to the optimal dispersion, highest Ru yields, and HER activity. W atoms regulate local electron structure and coordination environment, leading to faster proton supply and hydrogen release, thus achieving 10 mA cm⁻² at low overpotential of 27 mV (alkaline) and 66 mV (acidic). Notably, W_{0.05}-RuP₂@C₃N₄-NC maintains stability with staged 500–1000 mA cm⁻² for 1000 h in alkaline, and 1000 mA cm⁻² for ~300 h in acid, ascribing to the immobilized ultra-stable RuP₂ nanoclusters via EDTA-MF and metal-oxygen sites. The excellent activity and stability hold promise for industrial hydrogen production, which provides deeper insights into catalyst-support interaction and reasonable design of high Ru-loading electrocatalysts.

1. Introduction

Hydrogen is one of the most paramount important and environmentally benign alternatives to conventional fossil fuels. When combined with burgeoning fuel cell technology, hydrogen shows great potential to define a sustainable, clean and secure energy future [1,2]. Electrolytic water has emerged as an upcoming star to provide high value-added and high purity hydrogen with zero carbon emission. At present, platinum (Pt) noble-based materials are the best-performing benchmark (hydrogen evolution reaction) HER catalysts with the hydrogen absorption Gibbs free energies close to zero [3,4]. However, their application is severely limited by the scarcity and high cost, which compels materials scientists to search for relatively low-cost and high-performance electrocatalysts.

Currently, among Pt-free catalysts, nonprecious metal materials are popular candidates to replace precious metals but are still enormously hindered by inferior activity and stability [5,6]. Considering the excellent performance and much lower price to Pt (only ~4%), ruthenium (Ru) has aroused extensive interest from researchers as a promising HER

electrocatalyst [7–9]. To further bridge the gap between HER activity and cost, it is a more practical strategy to increase the yield and dispersion of Ru as much as possible under the premise of the same amount of Ru source. To this end, uniformly distributed and high-density Ru species are the most desirable [10,11]. To reach this target, compared with single atoms that are inclined to agglomerate caused by higher surface energy, highly dispersed and ultrafine Ru nanoclusters are potentially favorable, which can expose plenty of active sites and guarantee long-term durability. As proof, Zhou et al. found that larger RuP nanoparticles exhibit a surprisingly higher intrinsic activity and durability than small RuP nanoparticles [12]. Therefore, immobilized Ru-based nanoclusters with uniform distribution and small size are desired to realize simultaneous high activity and high stability. Whereas, due to the restriction of synthetic approaches and the immaturity of scale control technology, it is difficult to engineer the targeted nanoclusters and adjustable structure [13,14]. Moreover, isolated metal atoms are peculiarly prone to aggregate during high-temperature treatment. The main challenge is posed on the balance of load and catalytic performance. In this regard, choosing appropriate ligands to

* Corresponding authors.

E-mail addresses: dongbin@upc.edu.cn (B. Dong), ymchai@upc.edu.cn (Y.-M. Chai).

<https://doi.org/10.1016/j.apcatb.2021.120917>

Received 3 October 2021; Received in revised form 24 October 2021; Accepted 7 November 2021

Available online 22 November 2021

0926-3373/© 2021 Published by Elsevier B.V.

form stable chelates with Ru ions to hoist dispersion and optimize content is deemed as an effective strategy [14–16].

Recently, the newly flourished Ru-based phosphates have presented exciting HER performance in wide pH [12,17–19]. Theoretical calculations show that the hydrogen adsorption free energy (ΔG_{H^*}) of Ru-based phosphates is closer to zero than that of metallic Ru [12]. In addition, it has been well-documented that catalytic performance can be enhanced by heteroatom doping, which can tailor the electronic structure and adsorption property on the surface. Meanwhile, from the perspective of industrial application, high current density ($\geq 500 \text{ mA cm}^{-2}$) at low overpotentials is urgently necessary [20,21]. Yet, the dissolution of Ru in the electrolyte is unavoidable and is even severe for nanosized particles [22,23]. In addition to the suitable support, the right selection of foreign atoms should be corrosion resistant and electronically adjustable. As such, high-valence metal tungsten (W) atom, which is featured with chemical stability in both acidic and alkaline environments as well as high tolerance to poisoning [23], is precisely chosen. Besides, the W atom can form the W-Ru bond to inhibit the diffusion and dissolution of Ru [14,24], thus, strict criteria for commercial durability may be satisfied. Furthermore, the atomic radius of the W atom (2.02 Å) is bigger than the Ru atom (1.89 Å), the original lattice tends to distort and induce the local electron redistribution, activating the neighboring Ru to be the active sites. The synergistic effect between the W and RuP_x to promote water dissociation has also been reported [25]. However, it is also daunting to dope W atom into host materials because of its propensity to be easily oxidized.

Based on all the above discussion, the ultrafine and highly dispersed W doped RuP_2 nanoclusters embedded on carbon sheet matrix have been successfully synthesized by the combination of coordination polymer and self-template strategy for HER. The catalyst-support interactions are investigated on various carbon substrates, and we find that the ethylene diamine tetraacetic acid (EDTA) and melamine-formaldehyde (MF) synergistically optimize the Ru loading and distribution. Taking Na_2WO_4 as the metal source, the oxygen-bridged $[\text{WO}_4]$ tetrahedral is self-reduced to W atom and then introduced into the lattice of RuP_2 , which tunes the electron arrangement of Ru atoms, and efficiently lower the water dissociation barrier and ΔG_{H^*} . The resulting $\text{W}_{0.05}\text{-RuP}_2@\text{EDTA-MF}$ shows superb HER activity with the overpotential of only 27 mV and 66 mV at 10 mA cm^{-2} in 0.5 M H_2SO_4 and 1 M KOH, respectively. More importantly, in 0.5 M H_2SO_4 , the $\text{W}_{0.05}\text{-RuP}_2@\text{EDTA-MF}$ yields a stable, high current density of 1 A cm^{-2} at $\sim 76 \text{ mV}$, which can maintain at least 300 h; in 1.0 M KOH, chronopotentiometry curve shows that that final catalysts can first stably operate 500 mA for $\sim 400 \text{ h}$ and then 1000 mA for $\sim 600 \text{ h}$, which results from the limited Ru leaching by robust W-Ru bond and carbon carrier. This work provides a rational self-template and self-reduction strategy to design ultrafine nanocluster catalyst with simultaneous high activity and long-term stability at industrial, large current densities for water splitting systems.

2. Experimental section

2.1. Synthesis of $\text{Ru}_x@\text{EDTA-MF}$ and $\text{W}_y\text{-Ru}@ \text{EDTA-MF}$

The $\text{Ru}_x@\text{EDTA-MF}$ and $\text{W}_{0.05}\text{-Ru}@ \text{EDTA-MF}$ were synthesized by the self-template method. Taken $\text{W}_y\text{-Ru}@ \text{EDTA-MF}$ as an example, 0.5 g melamine, 0.74 g EDTA, 0.1 g RuCl_3 , and $\text{Na}_2\text{WO}_4 \cdot 2\text{H}_2\text{O}$ were dissolved into 20 mL deionized water and stirred for 20 min. Then, after adding 7.5 mL of formaldehyde, the above solution was heated at 80°C for 6 h under constant stirring. Finally, the white $\text{W}_y\text{-Ru}@ \text{EDTA-MF}$ (y is the mass of $\text{Na}_2\text{WO}_4 \cdot 2\text{H}_2\text{O}$) powder was obtained after heating at 80°C to evaporate the solvent.

The synthesis of $\text{Ru}_x@\text{EDTA-MF}$ (x is the mass of RuCl_3) is as with $\text{W}_y\text{-Ru}@ \text{EDTA-MF}$ without adding $\text{Na}_2\text{WO}_4 \cdot 2\text{H}_2\text{O}$.

2.2. Synthesis of $\text{Ru}_x\text{P}_2@\text{C}_3\text{N}_4\text{-NC}$ and $\text{W}_y\text{-RuP}_2@\text{C}_3\text{N}_4\text{-NC}$

The obtained $\text{Ru}_x@\text{EDTA-MF}$ and $\text{W}_y\text{-Ru}@ \text{EDTA-MF}$ were placed upstream of tubular a furnace and calcined at 900°C for 4 h with $\text{NaH}_2\text{PO}_4 \cdot \text{H}_2\text{O}$ downstream under Ar atmosphere, the final black power was named as $\text{Ru}_x\text{P}_2@\text{EDTA-MF}$ and $\text{W}_y\text{-RuP}_2@\text{EDTA-MF}$, respectively.

2.3. Synthesis of $\text{RuP}_2@\text{ME}$, $\text{RuP}_2@\text{MF}$, $\text{RuP}_2@\text{EDTA}$, $\text{RuP}_2@\text{EDTA-ME}$

The synthesis of $\text{RuP}_2@\text{ME}$, $\text{RuP}_2@\text{MF}$, $\text{RuP}_2@\text{EDTA}$, and $\text{RuP}_2@\text{ME-EDTA}$ were similar to $\text{Ru}_x\text{P}_2@\text{C}_3\text{N}_4\text{-NC}$ except replacing EDTA, melamine-formaldehyde with melamine, EDTA, MF, melamine-EDTA, respectively.

3. Results and discussion

3.1. Morphology and structure

A schematic diagram illustrating the synthesis process of the $\text{W}_{0.05}\text{-RuP}_2@\text{C}_3\text{N}_4\text{-NC}$ catalyst is presented in Fig. 1, which includes moderate reflux followed by a pyrolysis reduction. In detail, the oxygen-bridged $[\text{WO}_4]$ tetrahedral is employed as the W source [26]; the extra O can also be partially introduced to form a metal-O band. Here, the Melamine-formaldehyde resin (MF) and EDTA play a key role in dispersion improvement [14]. Specifically, MF is composed of abundant secondary and tertiary amine groups that can not only effectively chelate Ru/W ions (Fig. S1), but also can serve as the nitrogen source. Similarly, in addition to nitrogen, EDTA provides four carboxyl groups to coordinate with Ru/W ions [27]. During the calcination process, EDTA is cracked to C_xN_y template and subsequently uniformly assembled with obtained melamine hydroxymethyl compounds via intermolecular interactions. The C_3N_4 mainly comes from the uncoordinated melamine, as is shown in Fig. S2. The sodium tungstate dihydrate and Ru ions connect to the C_3N_4 matrix through hydrogen bonds and electrostatic forces to avoid agglomeration based on self-assembly chemistry. In detail, the $\text{Na}_2\text{WO}_4 \cdot 2\text{H}_2\text{O}$ and RuCl_3 were added to the EDTA-MF suspension. Then, during the hydrothermal process, the protonation of epoxy occurred to generate the positively charged carbon matrix. In the mild acidic solution, the protonation motivated W (VI) oxo in WO_4^{2-} fragment to transform to W hydroxo and finally to W aqua ligands, retaining the tetrahedral coordination. The W species could be captured and stabilized by protonated EDTA-ME sheets as a counterion without any additives due to the intensive coupling of negatively charged W anions and positively charged protonated EDTA-ME. The Ru can also be electrostatically attracted near the W site, thus leading to the signal disperse of Ru and W in the target catalyst. Finally, the uniform W-Ru was obtained by ammonia annealing. During this process, the reduction of EDTA-ME and N doping occurred simultaneously. Further, in order to enhance HER activity, the above $\text{W}_{0.05}\text{-Ru}@ \text{C}_3\text{N}_4\text{-NC}$ was treated with gas-phase phosphating. It is remarkable that the electron transfer or polarization may occur on the interface between the carbon network and W-RuP clusters. In this circumstance, the charge density of the atoms in the cluster can be changed. This phenomenon is referred to as metal-support interaction, which has been applied by chemists in constructing the proper active sites for HER [28].

Fig. S3 shows the Raman spectrum of catalyst before and after phosphorization; the I_D/I_G value sharply increased from 0.85 for $\text{W}_{0.05}\text{-Ru}@ \text{C}_3\text{N}_4\text{-NC}$ to 1.09 for $\text{W}_{0.05}\text{-RuP}_2@\text{C}_3\text{N}_4\text{-NC}$, suggesting the introduction of P can induce more intrinsic disorders. Previous reports have proved that the stress is derived from the lattice mismatch and is a favorable route to reflect and adjust the electronic structure on the surface of materials [27,29]. Fig. S4 shows the distinct stress enhancement after W or P introduction, which is admissible evidence for the adjusted electron distribution of $\text{W}_{0.05}\text{-RuP}_2@\text{C}_3\text{N}_4\text{-NC}$.

X-ray diffraction (XRD) patterns (Fig. 2a) are studied to analyze the

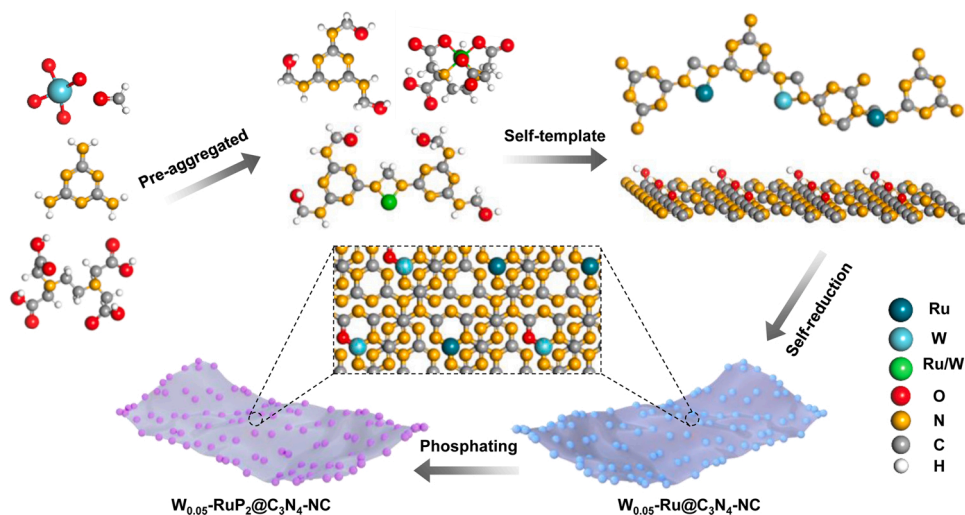


Fig. 1. Schematic illustration of the preparation process of $W_{0.05}\text{-RuP}_2@\text{C}_3\text{N}_4\text{-NC}$ catalyst.

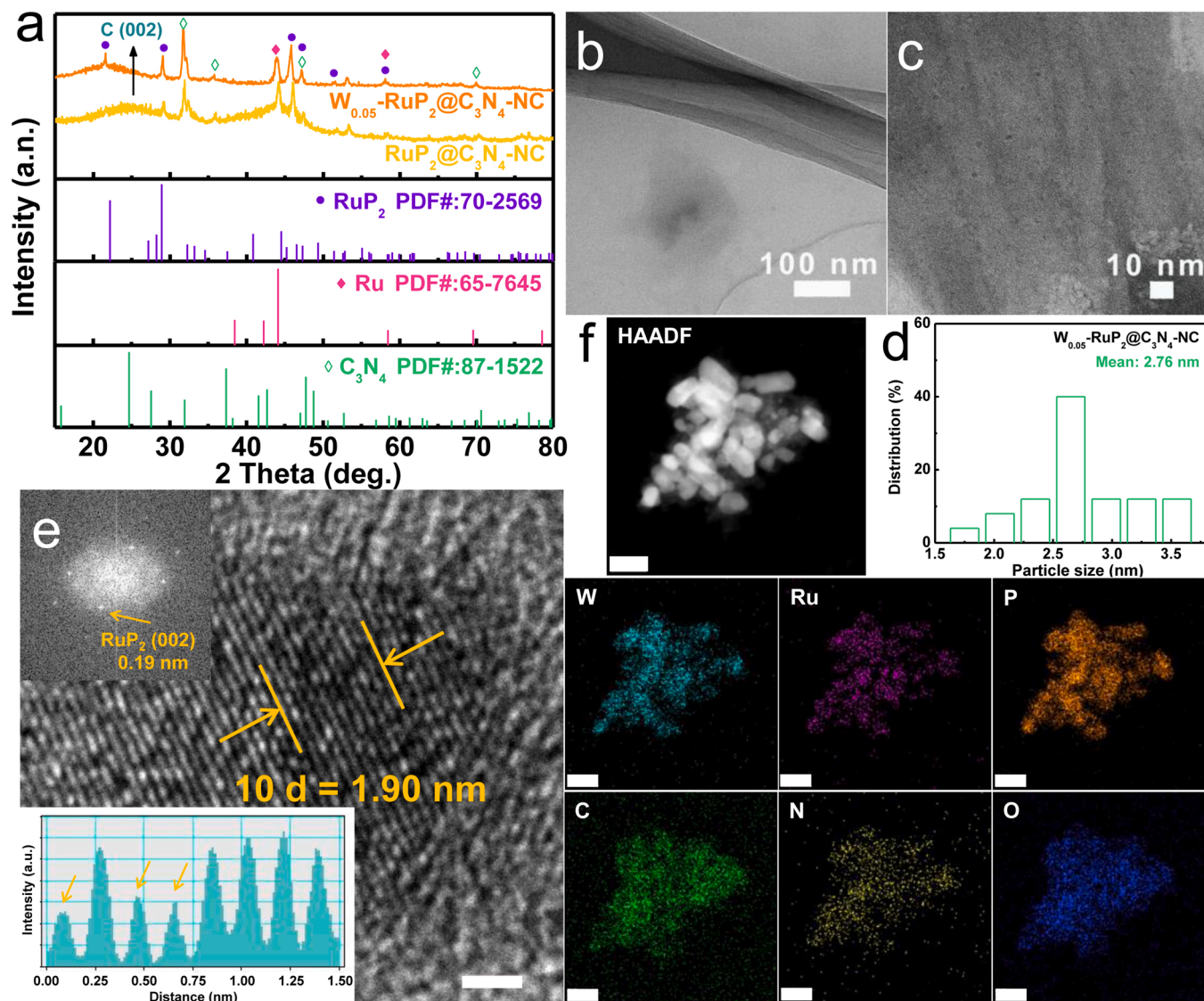


Fig. 2. Morphology characterization of final $W_{0.05}\text{-RuP}_2@\text{C}_3\text{N}_4\text{-NC}$ nanoclusters. (a) XRD patterns of $W_{0.05}\text{-Ru@C}_3\text{N}_4\text{-NC}$ and $W_{0.05}\text{-RuP}_2@\text{C}_3\text{N}_4\text{-NC}$. TEM images of (b) $\text{C}_3\text{N}_4\text{-NC}$ and (c) $W_{0.05}\text{-RuP}_2@\text{C}_3\text{N}_4\text{-NC}$ and corresponding particle distribution (d). (e) HRTEM and FFT, atomic intensity profile of $W_{0.05}\text{-RuP}_2@\text{C}_3\text{N}_4\text{-NC}$. Scale bar: 1 nm. (f) HAADF images of $W_{0.05}\text{-RuP}_2@\text{C}_3\text{N}_4\text{-NC}$. Scale bar: 50 nm.

structure of $\text{Ru}@C_3N_4\text{-NC}$ and $\text{W}_{0.05}\text{-Ru}@C_3N_4\text{-NC}$. The six characteristic peaks at 21.5° , 29.1° , 45.8° , 47.2° , 51.5° and 58.1° belonging to the (110), (101), (220), (002), (221) and (040) crystal planes of RuP_2 (PDF#: 70–2569), respectively. The response of the carbon template can also be identified: the broad diffraction peaks around 25.0° can be indexed to the (002) plane of graphitic carbon [14]. The obvious strong peaks of C_3N_4 can be observed at 31.7° , 35.8° , 47.1° and 70.0° (PDF#: 87–1522). The XRD signal of metallic Ru is also discerned possibly due to incomplete phosphating (PDF#: 65–7645). Notably, no W-related peaks can be recognized, in addition, after W substitution, the XRD pattern of $\text{W}_{0.05}\text{-RuP}_2@C_3N_4\text{-NC}$ shows an obvious negative shift, implying that a part of Ru with a smaller radius is successfully replaced by W with a larger radius. The morphology and structure of fabricated samples are characterized by scanning electron microscope (SEM) and transmission electron microscope (TEM). As displayed in Fig. 2b and c, the ultrafine W doped RuP_2 nanoparticles are homogeneously anchored on the C_3N_4 and NC thin layers in $\text{W}_{0.05}\text{-RuP}_2@C_3N_4\text{-NC}$ with an average diameter of approximately 2.76 nm (Fig. 2d). The high-resolution TEM (HRTEM) combined with the fast Fourier transform (FFT) images demonstrate more intuitive structure features of target $\text{W}_{0.05}\text{-RuP}_2@C_3N_4\text{-NC}$ and other comparable samples (Fig. 2e). The clear lattice fringe with a d-spacing of 1.90 Å is related to the (002) crystal plane of RuP_2 , which is in agreement with the XRD result. FFT also supplies the lattice spacing of 1.90 Å indexed to the (002) plane of RuP_2 . Clearly, there is no W-derived lattice perceived on the surface of $\text{W}_{0.05}\text{-RuP}_2@C_3N_4\text{-NC}$, which suggests the absence of W-related species

again. The discontinuous atomic arrangement in crystalline regions is a reflection of W doping, as demonstrated by the peak valleys of the atomic intensity profile (inset in Fig. 2e) [30]. The uniform distribution of Ru and W over the entire carbon nanosheets is corroborated by high-angle annular dark-field scanning TEM (HAADF-STEM) in Fig. 2f. The W and Ru contents in this sample are determined to be 15.09% and 15.39% by inductively coupled plasma mass spectrometry (ICP-MS). Moreover, the $\text{W}_{0.10}\text{-RuP}_2@C_3N_4\text{-NC}$ is also prepared to gain an insight into the role of the W atom for nanocluster dispersion and HER performance. According to Fig. S5, nanoparticle aggregates of about 10 nm begin to appear, perhaps due to insufficient available coordination sites, which could be bound to cover many active sites. To reveal the catalyst-support interactions for this system, the $\text{RuP}_2@ME$, $\text{RuP}_2@MF$, $\text{RuP}_2@EDTA$, and $\text{RuP}_2@EDTA\text{-ME}$ are also synthesized using melamine, MF, EDTA, melamine-EDTA as the various carbon substrates. As Fig. S6 shows, melamine alone has little dispersion effect on RuP_2 , HRTEM image contains a clear (111) crystal of RuP_2 with the lattice distance of 2.77 Å. Similar unsatisfactory dispersion can be seen from the case of sole MF, EDTA as chelating agent, the average particle size is about 15.23 nm and 8.05 nm, respectively (Fig. S7). Noticeably, the RuP_2 nanoparticles obtained by using ME and EDTA together as the dispersant ($\text{RuP}_2@EDTA\text{-ME}$) are significantly smaller and more uniform but still inferior to $\text{RuP}_2@C_3N_4\text{-NC}$ (Fig. S8). The morphologies of these contrast samples manifest the synergistic effect of EDTA and ME/MF on catalyst dispersion. Ru concentration in $\text{RuP}_2@EDTA\text{-ME}$ and $\text{RuP}_2@C_3N_4\text{-NC}$ is also investigated (Fig. S9, Table S1). With the

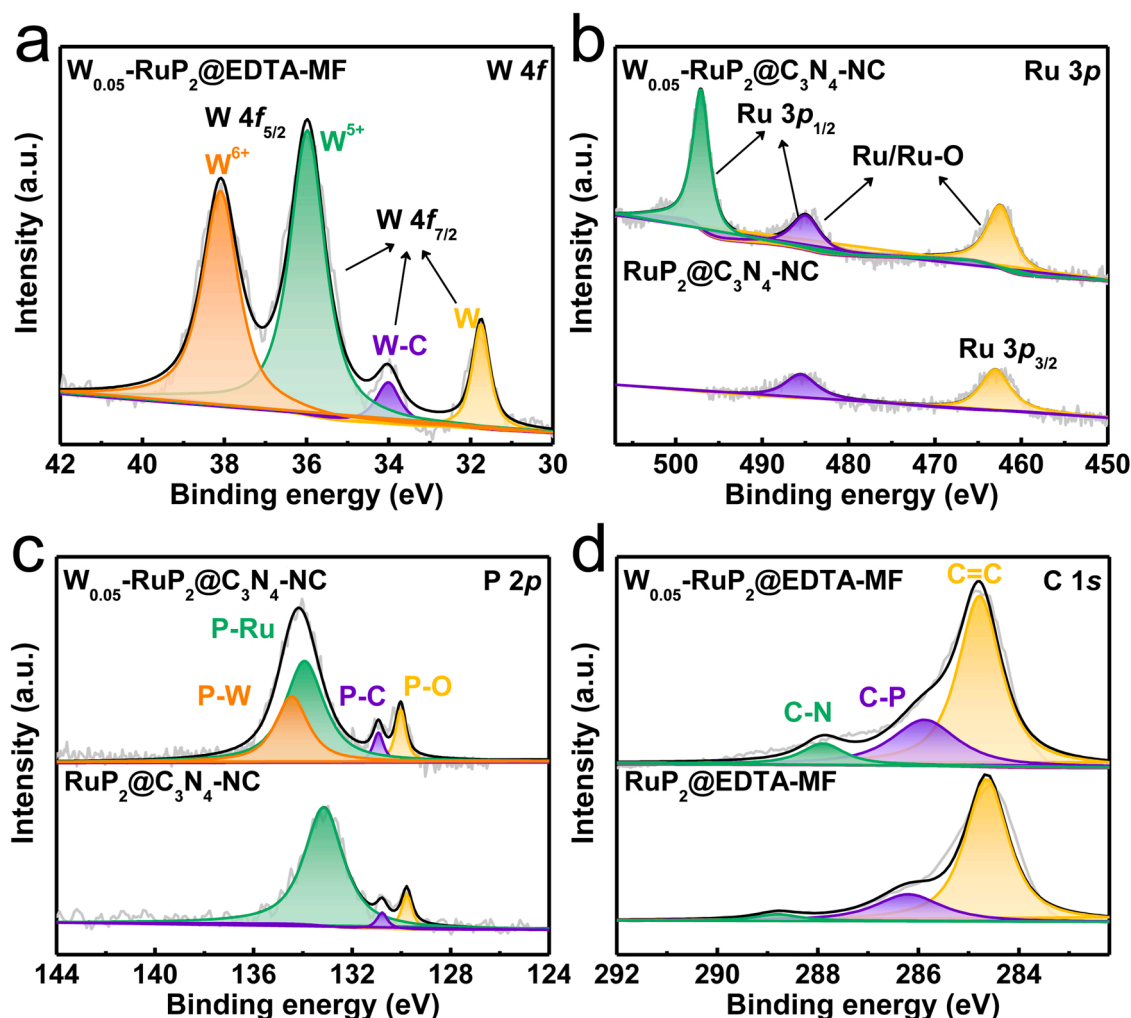


Fig. 3. XPS spectra of $\text{RuP}_2@C_3N_4\text{-NC}$ and $\text{W}_{0.05}\text{-RuP}_2@C_3N_4\text{-NC}$ sample. (a) W 4f, (b) Ru 3p, (c) P 2p, (d) C 1s.

same mass of RuCl_3 , the Ru loading of $\text{RuP}_2@\text{C}_3\text{N}_4\text{-NC}$ is higher, indicating less Ru loss, and the corresponding HER performance should be better. It should be noted that the abnormally high level of Ru (84.82 at %) in $\text{RuP}_2 @\text{ME}$ is mainly because ME begins to sublime in large quantities when the temperature exceeds 200°C [31], thus resulting in relatively low C content and high Ru content. According to all these morphologies results, it is worth mentioning that $\text{W}_{0.05}\text{-RuP}_2@\text{C}_3\text{N}_4\text{-NC}$ owns the best RuP_2 dispersion result from the fact that during annealing, $[\text{WO}_4]$ can form W-O weak ligand to effectively restrain the generation of RuP_2 bulks [14,24,26].

X-ray photoelectron spectroscopy (XPS) is carried out to deeply explore the valence state and local coordination chemistry of $\text{W}_{0.05}\text{-RuP}_2@\text{C}_3\text{N}_4\text{-NC}$. The coexistence of W, Ru, P, C, and N elements is verified by the XPS survey scan spectrum (Fig. S10a). Fig. 3a gives the XPS spectrum of W 4f, where the fitted W $4f_{7/2}$ and W $4f_{5/2}$ peaks at 31.7, 34.0, 36.0, and 38.1 eV come from metallic W, W coordinated with C, W^{5+} and W^{6+} , respectively [14,20,24]. Ru $3p_{3/2}$ and Ru $3p_{1/2}$ can be found at 462.4, 484.9 and 497.2 eV, and Ru $3d_{5/2}$ is located at 280.4 eV (Fig. 3b) [27,32]. The peaks at 462.4 and 484.9 eV are ascribed to metallic Ru or Ru-O species. In P 2p regions (Fig. 3c), the simulated peaks at 130.0, 130.9, 133.8 and 134.8 eV are the signals of P-O, P-C, P-Ru, and P-W, respectively [27,33]. With W incorporation, the binding energies of Ru 3p suffer from a negative movement while P 2p peaks show a positive movement, which means W atoms have effectively tailored the local electron configuration. For C 1s spectrum (Fig. 3d), the three deconvoluted peaks can be attributed to C=C (284.9 eV), C-P (286.3 eV) and C-N (288.0 eV), respectively [19,34]. N 1s region (Fig. S10b) shows the detected samples contain three different N species: metal (M)-N/pyridinic-N, pyrrolic-N, and graphitic-N at 397.0, 401.5, and 404.7 eV [14,19]. The different binding energies of C 1s and N 1s before and after W replacement are another powerful proof for the catalyst-support interactions. O 1s spectrum (Fig. S10c) exhibits three peaks at 531.1, 531.9, and 533.1 eV assigned to M-O, C=O, and C-O, respectively; this result confirms the presence of W-O groups in $\text{W}_{0.05}\text{-RuP}_2@\text{C}_3\text{N}_4\text{-NC}$, and the M-O sites are regarded to inhibit the agglomeration of metal atoms [19,24,26]. Incidentally, the valence states changes of $\text{W}_{0.05}\text{-RuP}_2 @\text{C}_3\text{N}_4\text{-NC}$ before and after P introduction are also detected (Fig. S11). After phosphating, the W 4f, Ru 3p, and Ru 3d peaks all positively shift to higher binding energy, further suggesting the rearrangement electron distribution on the surface of $\text{W}_{0.05}\text{-RuP}_2@\text{C}_3\text{N}_4\text{-NC}$ by P introduction. Analogously, the intimate electron interaction between carbon matrix and catalyst body is confirmed again by this changed XPS spectra (W 4f, Ru 3p, Ru 3d, and P 2p) combined with C 1s and N 1s peaks. Coupled with the following experiments, all these are propitious for the electrocatalytic performance boost.

3.2. Electrochemical performances

As proposed above, the dispersion and loading of active (W-)RuP₂ hinge on its catalyst-support interaction with various carbon templates and are intertwined with catalytic performances. Herein, the electrochemical HER activity of $\text{W}_{0.05}\text{-RuP}_2@\text{C}_3\text{N}_4\text{-NC}$ and other control samples is evaluated in the 1.0 M KOH solution by means of a three-electrode system. As can be seen from Fig. S12a, $\text{RuP}_2 @\text{EDTA}$, $\text{RuP}_2@\text{ME}$, and $\text{RuP}_2@\text{EDTA-ME}$ all show bigger onset overpotential and poorer HER activity, which mainly due to the worse dispersion of RuP_2 on this supports, as previously demonstrated by TEM images in Figs. S6-S8. $\text{RuP}_2@\text{C}_3\text{N}_4\text{-NC}$ owns a much smaller onset overpotential of 4.0 mV, suggesting excellent electrocatalytic activity. Moreover, among these contrast samples, $\text{RuP}_2@\text{C}_3\text{N}_4\text{-NC}$ has the smallest overpotential at the current density of 10 mA cm^{-2} (44.7 mV), which proves the as-mentioned vital role of uniform distribution of active center in HER enhancement. It should be noted that the collaboration of EDTA and ME ligands leads to a higher yield of RuP_2 when the same quality RuCl_3 is used as Ru source, as confirmed by content detection in Table S1. EDTA-

MF carrier is adopted to further study the influence of Ru content upon HER performance, the mass of RuCl_3 reagent is adjusted. Fig. S12b suggests 0.10 g is the optimized mass for the Ru source. We can reasonably posit that EDTA-MF can not provide sufficient accessible chelation sites for Ru; besides, the agglomerate property is still a headache for Ru nanocluster catalysts. Precious researches have found that the tungsten-oxygen cluster can serve as weak coordination carriers for metals during the in-situ carbonization process, thus effectively preventing the formation of metals bulk [35]. In addition, metallic W possesses unsaturated d-orbital with variable valence states and can act as a favorable doping metal for HER catalysts. Therefore, the $[\text{WO}_4]$ is chosen to further elevate HER performance.

Encouragingly, Fig. 4a shows that appropriate W doping can greatly enhance hydrogen evolution activity of $\text{W}_{0.05}\text{-RuP}_2@\text{C}_3\text{N}_4\text{-NC}$, which only requires 27 mV to reach 10 mA cm^{-2} with low onset overpotential of 2.0 mV, superior to commercial Pt/C benchmark and other reported RuP_2 catalysts (Fig. 4b, Table S2). The LSV of $\text{W}_{0.05}\text{-RuP}_2@\text{C}_3\text{N}_4\text{-NC}$ normalized by the mass of Ru is calculated to be mA/mg_{Ru} at -0.07 V , which is 16 times that of commercial Pt/C at the same potential (Fig. S13). A smaller Tafel slope is also an indicator of the good activity of electrocatalysts. As expected, RuP_2 on different carbon carriers shows different Tafel slopes, where $\text{RuP}_2@\text{C}_3\text{N}_4\text{-NC}$ has a relatively lower slope value of 99.3 mV dec^{-1} (Fig. 4c), after W incorporation, the Tafel slope further decreases to 84.0 mV dec^{-1} , suggesting the HER kinetics have been greatly boosted. These slope values between 40 and 120 mV dec^{-1} imply the Volmer-Tafel mechanism as the HER pathway, in which the recombination of chemisorbed hydrogen atoms governs the HER reaction rate [20,36]. Exchange current density (J_0) is another critical parameter reflecting electron transfer rate between electrode and catalyst surface [37]. The calculated J_0 of $\text{W}_{0.05}\text{-RuP}_2@\text{C}_3\text{N}_4\text{-NC}$ is 3.4 mA cm^{-2} , which is better than $\text{RuP}_2@\text{C}_3\text{N}_4\text{-NC}$ (1.4 mA cm^{-2}) and Pt/C (2.1 mA cm^{-2}) (Fig. 4d). Clearly, the intrinsic catalytic activity of $\text{W}_{0.05}\text{-RuP}_2@\text{C}_3\text{N}_4\text{-NC}$ with well-dispersed small-sized RuP_2 nanoclusters performs best in 1.0 M KOH [37,38]. Turnover frequency (TOF) is applied as a merit index to evaluate HER electrocatalysts [36,38]. The yield $\text{W}_{0.05}\text{-RuP}_2@\text{C}_3\text{N}_4\text{-NC}$ sample exhibits a larger TOF of $3.8 \text{ H}_2 \text{ s}^{-1}$ under overpotential of 100 mV (Fig. 4e), revealing better activity attributed to the high density of active RuP_2 and regulated electron donor-acceptor property by synergetic EDTA-MF coordination and foreign W replacement. Electrochemical surface area (ECSA) is assessed by the double-layer capacitance (C_{dl}) value that is calculated from respective cyclic voltammetry (CV) curves (Fig. S13a-e). As Fig. S15f shows, the C_{dl} of $\text{RuP}_2@\text{C}_3\text{N}_4\text{-NC}$ is 22.6 mF cm^{-2} , higher than $\text{RuP}_2@\text{EDTA-ME}$ (14.6 mF cm^{-2}), demonstrating that EDTA-MF is dedicated to the exposure of more active sites. While $\text{W}_{0.05}\text{-RuP}_2@\text{C}_3\text{N}_4\text{-NC}$ has the highest C_{dl} value of 26.8 mF cm^{-2} , which coupled with its normalized current density (Figs. S15 and S16) and smallest fitting semicircle diameter from electrochemical impedance spectroscopy (EIS) plots (Fig. 4f) prove the pivotal role of W/W-O in maximizing available active sites, enhancing intrinsic activity and interfacial electron transport capacity of $\text{W}_{0.05}\text{-RuP}_2@\text{C}_3\text{N}_4\text{-NC}$.

HER stability is a more interesting factor for commercial applications. To highlight the role of the W atom in operation stability, we collected the chronoamperometry curves of $\text{RuP}_2@\text{C}_3\text{N}_4\text{-NC}$ and $\text{W}_{0.05}\text{-RuP}_2@\text{C}_3\text{N}_4\text{-NC}$. Fig. S17 shows the severe degradation of $\text{RuP}_2@\text{C}_3\text{N}_4\text{-NC}$ and the super stable $i-t$ curve of $\text{W}_{0.05}\text{-RuP}_2@\text{C}_3\text{N}_4\text{-NC}$ attributed to the excellent corrosion resistance of W atoms. The final $\text{W}_{0.05}\text{-RuP}_2@\text{C}_3\text{N}_4\text{-NC}$ catalyst is coated onto nickel foam to measure the long-term stability at a large current density. The LSV curve is first collected and depicted in Fig. 5a; it can be seen that the HER activity is further obviously boosted, only 76 and 194 mV required at 100 and 1000 mA cm^{-2} , which can be attributed to the superior conductivity of nickel foam. This phenomenon further manifests the significance of faster electron transfer to the HER reaction.

After the 5000 cycle CV scan, the LSV curve of $\text{W}_{0.05}\text{-RuP}_2@\text{C}_3\text{N}_4\text{-NC}$ only shows slight degradation (Fig. 5b). Further, the $V-t$ relations are

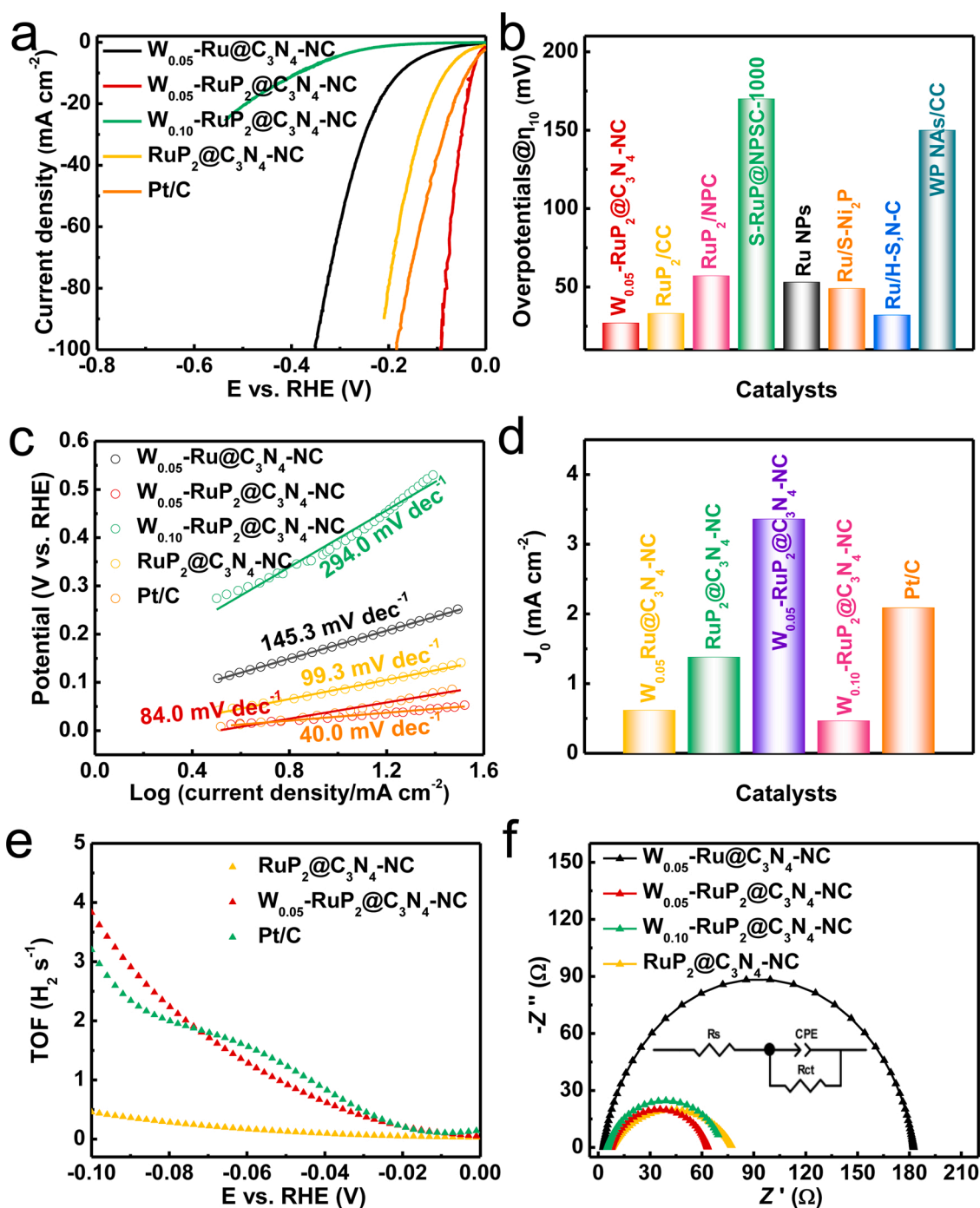


Fig. 4. Electrocatalytic HER performance of obtained catalysts in 1.0 M KOH solution. (a) HER polarization curves of W_{0.05}-Ru@C₃N₄-NC, W_{0.05}-RuP₂@C₃N₄-NC, W_{0.10}-RuP₂@C₃N₄-NC, RuP₂@C₃N₄-NC, Pt/C catalysts. (b) In 1.0 M KOH solution, Tafel slopes and overpotentials at 10 mA cm⁻² compared with the recently reported HER catalysts. (c) Tafel plots obtained from the polarization curves in (a). (d) Comparison of exchange current density. (e) The potential-dependent TOF curves. (f) EIS plots.

recorded by two-step chronopotentiometry in Fig. 5c which displays that the current density keeps stable at first 500 for ~400 h and then 1000 mA cm⁻² for ~600 h. Furthermore, the nanocluster morphology and crystalline structure of W_{0.05}-RuP₂@C₃N₄-NC remain almost unchanged (Fig. S18). The intriguing durability mainly results from the carbon carrier and metal-O sites which can effectively refrain from the existence of catalyst blocks. Taken together, the W_{0.05}-RuP₂@C₃N₄-NC catalyst shows the robust structure and excellent stability for hydrogen evolution in alkaline media.

The HER performance of obtained materials is also measured in

0.5 M H₂SO₄. Similar to the activity in alkaline environments, RuP₂@C₃N₄-NC is the best-performing sample with the aid of EDTA-MF chelating agents (Fig. S19). Moreover, Ru contents also have an impact on catalytic activity analogous to that in 1.0 M KOH. With incorporating W/W-O groups, excitingly, it only requires a low overpotential of 66 mV to reach 10 mA cm⁻², comparable to other reported RuP₂ catalysts (Fig. 6a and b). Meanwhile, W_{0.05}-RuP₂@C₃N₄-NC shows the smallest Tafel slope value of 41.1 mV dec⁻¹ and largest J₀ of 0.34 mA cm⁻¹, suggesting fast HER kinetics (Fig. 6c and d).

In addition to overpotentials at 10 mA cm⁻², TOF is calculated

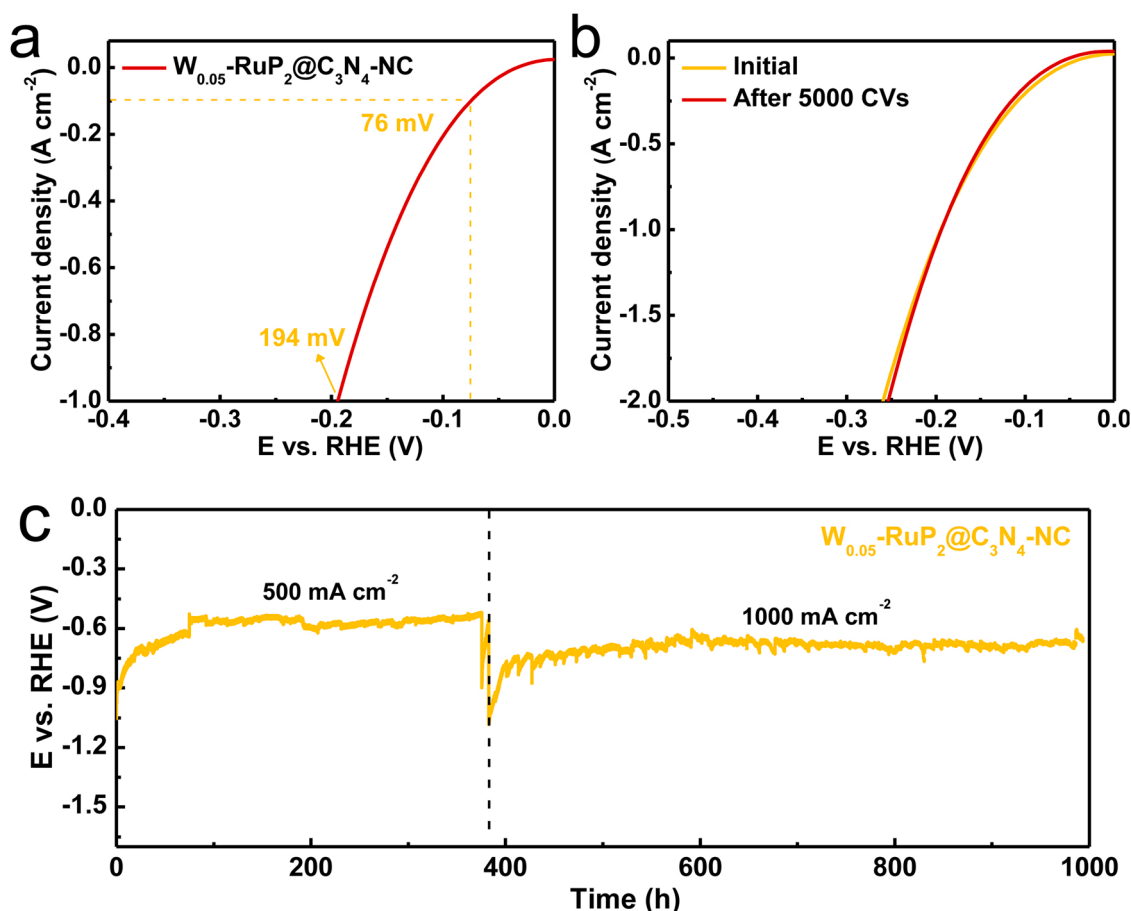


Fig. 5. (a) LSVs for W_{0.05}-RuP₂@C₃N₄-NC coated on nickel foam in 1.0 M KOH solution. (b) Polarization curves for W_{0.05}-RuP₂@C₃N₄-NC before and after 5000 CV cycles. (c) The v - t curves for W_{0.05}-RuP₂@C₃N₄-NC at 500 mA cm⁻² for ~400 h and 1000 mA cm⁻² for ~600 h.

according to the estimated number of active sites in Fig. 6e. The much higher TOF of 1.4 H₂ s⁻¹ at 100 mV together with standardized current density by ECSA reveals the remarkable intrinsic activity of W_{0.05}-RuP₂@C₃N₄-NC (Figs. S20–22). Besides, EIS plots fitted by the equivalent circuit in Fig. 6f, substantiate its admirable electron mobility. More importantly, no clear overpotential enhancement can be discerned for LSV of W_{0.05}-RuP₂@C₃N₄-NC catalyst after the fast 5000 CV test (Fig. 6g). Chronopotentiometric curves demonstrate that W_{0.05}-RuP₂@C₃N₄-NC can stably operate 500 h at the high current density of 1000 mA cm⁻² without distinct catalyst agglomeration and distinct lattice mismatch (Fig. 6h and Fig. S23). All these experimental results indicate that the catalyst-support interaction and W doping are both in favor of hydrogen evolution with long-term durability.

3.3. The study of structure-property relationship and mechanism

First-principles density functional theory (DFT) calculations are further carried out to uncover the reason underlying the excellent HER performance. To simplify simulation, the RuP₂ and W doped RuP₂ (W-RuP₂) models are constructed, as Fig. S24 shows. The density of state (DOS) explains the distribution of electrons at certain energies, where RuP₂ and W-RuP₂ both exhibit metallic properties. The DOS of Ru atom for W-RuP₂ is different from that of RuP₂ because of W doping, and electrons are closer to Fermi level for W-RuP₂ (Fig. 7a). The modified electron structure can also be corroborated by the electron density difference in Fig. S25. After being substituted by W atoms, the Ru atom suffers from increased electron density while the electron density of the P atom is decreased, which is coincided with XPS results.

Generally, the adjusted electron arrangement is bound to modulate

adsorption properties on the surface of W-RuP₂ [7,39]. As such, the Gibbs free energies in the whole HER pathways including adsorption of H₂O, dissociation of H₂O to produce adsorbed H (H*), the formation of adsorbed H₂ by the combination of H* and proton from H₂O, and desorption of H₂ from the surface are computed based on the (002) lattice plane (Figs. 7b and S26) [40–42]. As Fig. 7c manifests, on the cleaved surface, W-RuP₂ has lower Gibbs free energy for water dissociation (0.273 eV) than RuP₂ (0.270 eV). Furthermore, the dissociation of adsorbed H₂O into H and OH must be fast enough to provide accessible protons for H₂ generation. In this case, the dissociation of H₂O on the W-RuP₂ (002) plane is much easier (−0.32 eV) compared with RuP₂ (−0.29 eV), which may be thanks to the enrichment of electrons at the Ru site after W doping [25]. Metal-hydrogen (M-H) bond plays an imperative role in HER; too negative M-H binding energy should benefit the adsorption of hydrogen intermediate but unfavorable to the desorption of products, while too positive M-H binding energy is the opposite. Evidently, as can be seen from Fig. 7d, the ΔG_{H^*} on the surface of W-RuP₂ is 0.18 eV, much lower than that of RuP₂ (0.99 eV). This better ΔG_{H^*} could lead to accelerated proton adsorption, reduction process, and hydrogen release. Intrinsically, the calculated ΔG_{H^*} is closely related to d -band energy level, compared with RuP₂ (−1.39 eV), and appropriated d -band position of −0.58 eV closer to Fermi level for W-RuP₂ would induce stronger hydrogen adsorption, indicating that the H* adsorption is thermodynamically favorable (Fig. S27) [43–45]. In a nutshell, combined with the above experimental and theoretical results, the great HER performance of W_{0.05}-RuP₂@C₃N₄-NC is chalked up to the following reasons: (1) The EDTA and MF ligands synergistically promote the dispersion and high yields of ultrafine RuP₂ species, endowing W_{0.05}-RuP₂@C₃N₄-NC with abundant active sites. (2) The application of

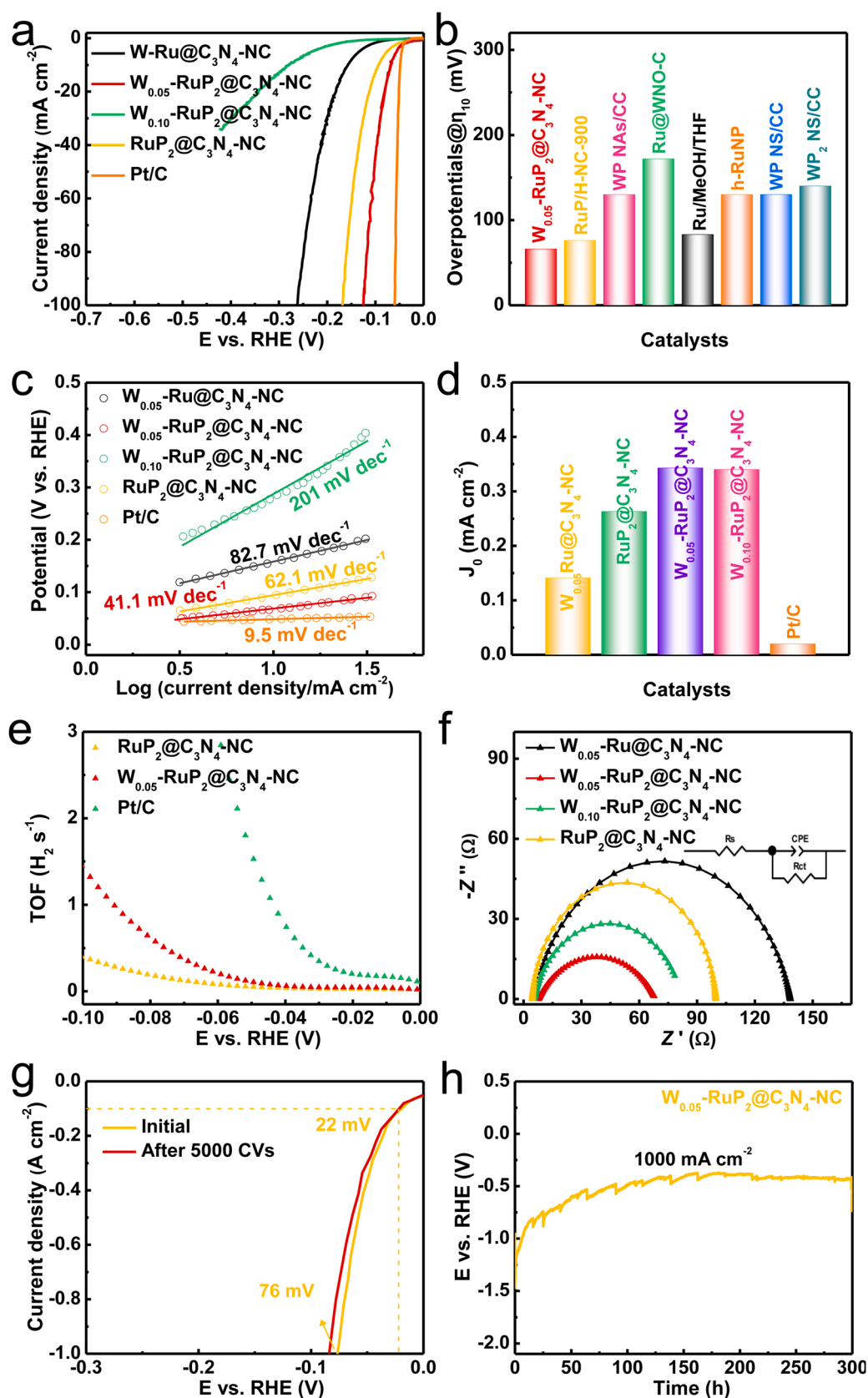


Fig. 6. Electrocatalytic HER performance of catalysts in 0.5 M H_2SO_4 . (a) HER polarization curves of $\text{W}_{0.05}\text{-Ru@C}_3\text{N}_4\text{-NC}$, $\text{W}_{0.05}\text{-RuP}_2\text{@C}_3\text{N}_4\text{-NC}$, $\text{W}_{0.10}\text{-RuP}_2\text{@C}_3\text{N}_4\text{-NC}$, $\text{RuP}_2\text{@C}_3\text{N}_4\text{-NC}$, Pt/C catalysts. (b) In 0.5 M H_2SO_4 solution, η Tafel slopes and overpotentials at 10 mA cm^{-2} compared with the recently reported HER catalysts. (c) Tafel plots obtained from the polarization curves in (a). (d) Comparison of exchange current density. (e) The potential-dependent TOF curves. (f) EIS plots. (g) Polarization curves for $\text{W}_{0.05}\text{-RuP}_2\text{@C}_3\text{N}_4\text{-NC}$ before and after 5000 CV cycles. (h) The ν -t curves for $\text{W}_{0.05}\text{-RuP}_2\text{@C}_3\text{N}_4\text{-NC}$ at 1000 mA cm^{-2} for $\sim 300 \text{ h}$.

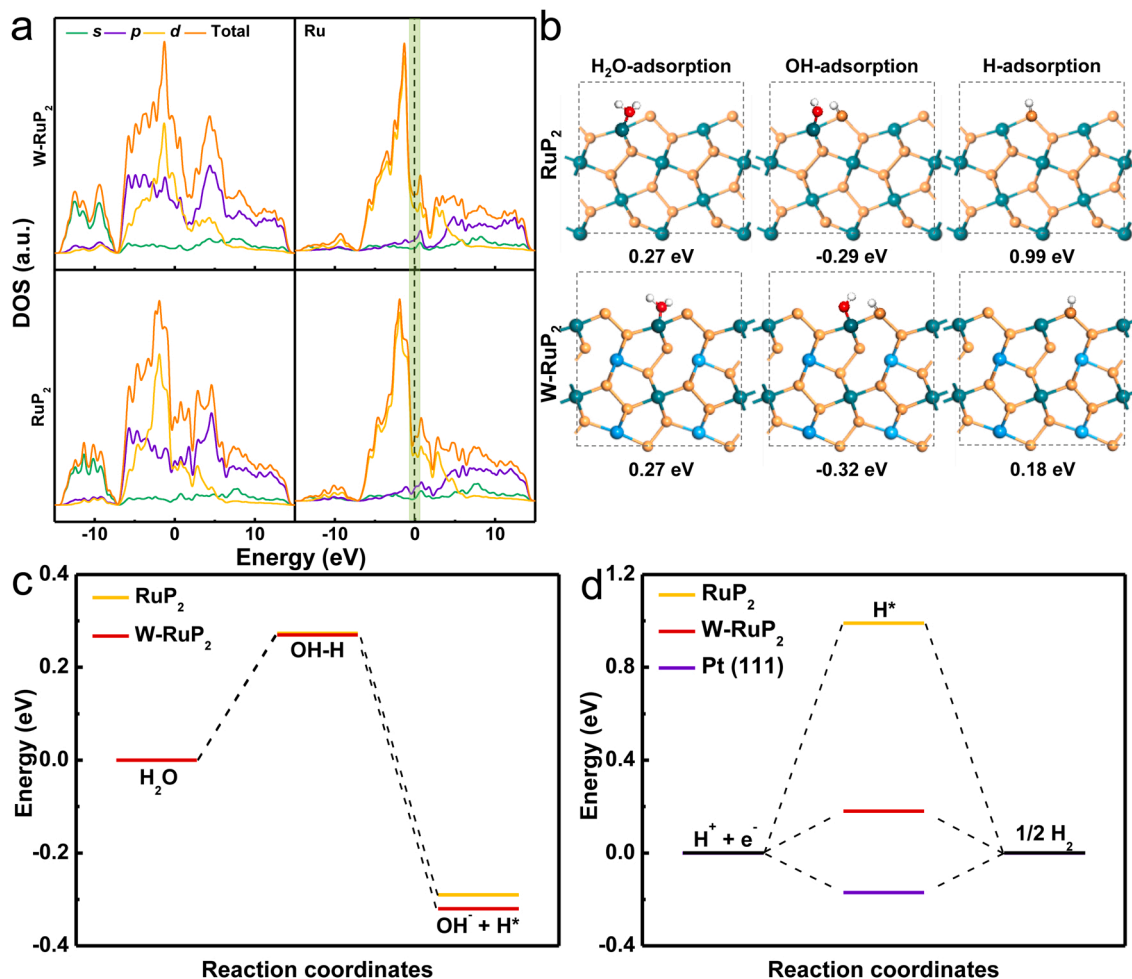


Fig. 7. (a) Calculated DOS for RuP₂ and W-RuP₂. The feimi level is set at 0 eV. (b) The HER pathways on the surface of RuP₂ and W-RuP₂. Blue ball: W; Dark green: Ru, Orange ball: P. Red ball: O; White ball: hydrogen. (c) The related kinetic energy barriers for water dissociation and (d) Calculated free-energy diagram of HER on the surfaces of RuP₂ and W-RuP₂.

[WO₄] can dope W into RuP₂ lattice, leading to faster electron transport, expedited water dissociation, and lower ΔG_{H^*} ; the induced metal-O sites act as weak ligand to prevent catalyst agglomeration. (3) The metallic active species integrating with in-situ generated ultrathin carbon matrix bestows enhanced conductivity and high electrochemical surface area, which guarantees the optimization of accessibility of active RuP₂ center and mass transfer in a heterogeneous catalytic system. (4) The EDTA-MF network and W-O cluster greatly reduce the agglomeration tendency of W_{0.05}-RuP₂@C₃N₄-NC during operation and maintain super stability.

4. Conclusion

In summary, we have designed an ultrafine RuP₂ electrocatalyst supported on biphasic carbon substrate for high-performance acidic and alkaline HER taking the catalyst-support interaction into account. As proved, multiple ligands are more conducive to the dispersion and long-term stability of the catalyst. The EDTA-MF ligand and subsequently introduced metal-O sites synergistically promote the uniform and high-density dispersion of RuP₂ nanoclusters. The W atoms finely tune the electron configuration and adsorption capability of the final W_{0.05}-RuP₂@C₃N₄-NC catalyst. Remarkably, the W_{0.05}-RuP₂@C₃N₄-NC exhibits low overpotential of 27 mV (alkaline) and 66 mV (acidic) at 10 mA cm⁻². Noticeably, the W_{0.05}-RuP₂@C₃N₄-NC also realize catalyzing water at large current density of staged 500–1000 mA cm⁻² for 1000 h in alkaline media and 1000 mA cm⁻² for ~300 h in acidic media, showing great potential for industrial applications, which

provides a new facile route for high-valence W doped and ultrafine nanoclusters via coordination effect.

CRediT authorship contribution statement

Ya-Nan Zhou: Data curation, Writing – original draft, Formal analysis, Investigation. **Fu-Li Wang:** Writing – original draft, Formal analysis. **Jun Nan:** Writing – review & editing, Formal analysis. **Bin Dong:** Formal analysis, Investigation, Resources, Writing – original draft, Funding acquisition, Project administration, Writing – review & editing. **Hui-Ying Zhao:** Writing – original draft. **Feng-Ge Wang:** Writing – review & editing, Methodology. **Ning Yu:** Methodology, Writing – review & editing. **Ren-Ni Luan:** Writing – original draft. **Da-Peng Liu:** Conceptualization, Writing – original draft, Supervision. **Yong-Ming Chai:** Funding acquisition, Conceptualization, Investigation, Resources, Formal analysis, Supervision, Writing – review & editing.

Declaration of Competing Interest

The authors declare that they have no known competing financial interests or personal relationships that could have appeared to influence the work reported in this paper.

Acknowledgments

This work is financially supported by National Natural Science Foundation of China (52174283) and Qingdao Science and Technology Benefiting People Special Project (20–3-4-8-nsh) and the Fundamental Research Funds for the Central Universities (20CX02212A) and the Development Fund of State Key Laboratory of Heavy Oil Processing and Postgraduate Innovation Project of China University of Petroleum (YCX2020046).

Appendix A. Supporting information

Supplementary data associated with this article can be found in the online version at doi:10.1016/j.apcatb.2021.120917.

References

- [1] J. Song, C. Wei, Z.F. Huang, C. Liu, L. Zeng, X. Wang, Z.J. Xu, A review on fundamentals for designing oxygen evolution electrocatalysts, *Chem. Soc. Rev.* 49 (2020) 2196–2214.
- [2] J. Zhou, L. Yu, Q. Zhou, C. Huang, Y. Zhang, B. Yu, Y. Yu, Ultrafast fabrication of porous transition metal foams for efficient electrocatalytic water splitting, *Appl. Catal. B: Environ.* 288 (2021), 120002.
- [3] Y. Ding, B.Q. Miao, S.N. Li, Y.C. Jiang, Y.Y. Liu, H.C. Yao, Y. Chen, Benzylamine oxidation boosted electrochemical water-splitting: Hydrogen and benzonitrile co-production at ultra-thin Ni₂P nanomeshes grown on nickel foam, *Appl. Catal. B: Environ.* 268 (2020), 118393.
- [4] C. Wei, Y. Sun, G.G. Scherer, A.C. Fisher, M. Scherburne, J.W. Ager, Z.J. Xu, Surface composition dependent ligand effect in tuning the activity of nickel–copper bimetallic electrocatalysts toward hydrogen evolution in alkaline, *J. Am. Chem. Soc.* 142 (2020) 7765–7775.
- [5] X. Wang, J. He, B. Yu, B. Sun, D. Yang, X. Zhang, Q. Zhang, W. Zhang, L. Gu, Y. Chen, CoSe₂ nanoparticles embedded MOF-derived Co–N–C nanoflake arrays as efficient and stable electrocatalyst for hydrogen evolution reaction, *Appl. Catal. B: Environ.* 258 (2019), 117996.
- [6] C. Huang, L. Yu, W. Zhang, Q. Xiao, J. Zhou, Y. Zhang, P. An, J. Zhang, Y. Yu, N-doped Ni–Mo based sulfides for high-efficiency and stable hydrogen evolution reaction, *Appl. Catal. B: Environ.* 276 (2020), 119137.
- [7] G. Meng, H. Tian, L.X. Peng, Z.H. Ma, Y.F. Chen, C. Chen, Z.W. Chang, X.Z. Cui, J. L. Shi, Ru to W electron donation for boosted HER from acidic to alkaline on Ru/WNO sponges, *Nano Energy* 80 (2021), 105531.
- [8] P.P. Su, W. Pei, X.W. Wang, Y.F. Ma, Q.K. Jiang, J. Liang, S. Zhou, J.J. Zhao, J. Liu, G.Q. Lu, Exceptional electrochemical HER performance with enhanced electron transfer between Ru nanoparticles and single atoms dispersed on a carbon substrate, *Angew. Chem. Int. Ed.* 60 (2021) 16044–16050.
- [9] Z. Liu, L.L. Zeng, J.Y. Yu, L.J. Yang, J. Zhang, X.L. Zhang, F. Han, L.L. Zhao, X. Li, H. Liu, W.J. Zhou, Charge redistribution of Ru nanoclusters on Co₃O₄ porous nanowire via the oxygen regulation for enhanced hydrogen evolution reaction, *Nano Energy* 85 (2021), 105940.
- [10] J. Yang, H. Guo, S.L. Chen, Y.L. Li, C. Cai, P. Gao, L.P. Wang, Y.N. Zhang, R.J. Sun, X.B. Niu, Z.M. Wang, Anchoring and space-confinement effects to form ultrafine Ru nanoclusters for efficient hydrogen generation, *J. Mater. Chem. A* 6 (2018) 13859–13866.
- [11] Y.L. Wu, X.F. Li, Y.S. Wei, Z.M. Fu, W.B. Wei, X.T. Wu, Q.L. Zhu, Q. Xu, Ordered macroporous superstructure of nitrogen-doped nanoporous carbon implanted with ultrafine Ru nanoclusters for efficient pH-universal hydrogen evolution reaction, *Adv. Mater.* 33 (2021), 2006965.
- [12] J. Yu, Y. n Guo, S.X. She, S.S. Miao, M. Ni, W. Zhou, M.L. Liu, Z.P. Shao, Bigger is Surprisingly Better: Agglomerates of Larger RuP Nanoparticles Outperform Benchmark Pt Nanocatalysts for the Hydrogen Evolution Reaction, *Adv. Mater.* 30 (2018), 1800047.
- [13] W. Fang, L. Huang, S. Zaman, Z. Wang, Y. Han, B.Y. Xia, Recent Progress on Two-dimensional Electrocatalysis, *Chem. Res. Chin. Univ.* 36 (2020) 611–621.
- [14] Y. Gu, B.J. Xi, W.Z. Tian, H. Zhang, Q. Fu, S.L. Xiong, Boosting selective nitrogen reduction via geometric coordination engineering on single-tungsten-atom catalysts, *Adv. Mater.* 33 (2021), 2100429.
- [15] D. Grasseschi, W.C. Silva, R.S. Paiva, L.D. Starke, A.S. Nascimento, Surface coordination chemistry of graphene: Understanding the coordination of single transition metal atoms, *Coord. Chem. Rev.* 422 (2020), 213469.
- [16] J. Li, Y.N. Zhou, W.J. Tang, J. Zheng, X.P. Gao, N. Wang, X. Chen, M. Wei, X. Xiao, W. Chu, Cold-plasma technique enabled supported Pt single atoms with tunable coordination for hydrogen evolution reaction, *Appl. Catal. B: Environ.* 285 (2021), 119861.
- [17] D. Zhang, H. Zhao, B. Huang, B. Li, H. Li, Y. Han, Z. Wang, X. Wu, Y. Pan, Y. Sun, X. Sun, J. Lai, L. Wang, Advanced Ultrathin RuPdM (M = Ni, Co, Fe) Nanosheets Electrocatalyst Boosts Hydrogen Evolution, *ACS Cent. Sci.* 5 (2019) 1991–1997.
- [18] Q.B. Chang, J.W. Ma, Y.Z. Zhu, Z. Li, D.Y. Xu, X.Z. Duan, W.C. Peng, Y. Li, G. L. Zhang, F.B. Zhang, X.B. Fan, Controllable Synthesis of Ruthenium Phosphides (RuP and RuP₂) for pH-Universal Hydrogen Evolution Reaction, *ACS Sustain. Chem. Eng.* 6 (2018) 6388–6394.
- [19] Z. Pu, I.S. Amini, Z. Kou, W. Li, S. Mu, RuP₂-based catalysts with platinum-like activity and higher durability for hydrogen evolution reaction at all pH values, *Angew. Chem. Int. Ed.* 56 (2017) 11559–11564.
- [20] R. Li, H.Y. Wang, F. Hu, K.C. Chan, X.J. Liu, Z.P. Lu, J. Wang, Z.B. Li, L.J. Zeng, Y. Y. Li, X.J. Wu, Y.J. Xiong, IrW nanochannel support enabling ultrastable electrocatalytic oxygen evolution at 2 Acm^{−2} in acidic media, *Nat. Commun.* 12 (2021) 3540.
- [21] J.Q. Zhang, X. Shang, H. Ren, J.Q. Chi, H. Fu, B. Dong, C.G. Liu, Y.M. Chai, Modulation of Inverse Spinel Fe₃O₄ by Phosphorus Doping as an Industrially Promising Electrocatalyst for Hydrogen Evolution, *Adv. Mater.* 31 (2019), 1905107.
- [22] X.K. Kong, K. Xu, C.L. Zhang, J. Dai, S.N. Oliaee, L.Y. Li, X.C. Zeng, C.Z. Wu, Z. M. Peng, Free-standing two-dimensional Ru nanosheets with high activity toward water splitting, *ACS Catal.* 6 (2016) 1487–1492.
- [23] W.Z. Tu, K. Chen, L.J. Zhu, H.C. Zai, B. E. X.X. Ke, C.F. Chen, M.L. Sui, Q. Chen, Y. J. Li, Tungsten-doping-induced surface reconstruction of porous ternary Pt-based alloy electrocatalyst for oxygen reduction, *Adv. Funct. Mater.* 29 (2019), 1807070.
- [24] Y. Yang, Y.M. Qian, H.J. Li, Z.H. Zhang, Y.W. Mu, D. Do, B. Zhou, J. Dong, W. J. Yang, Y. Qin, L. Fang, R.F. Feng, J.G. Zhou, P. Zhang, J.C. Dong, G.H. Yu, Y.Y. Liu, X.M. Zhang, X.J. Fan, O-coordinated W–Mo dual-atom catalyst for pH-universal electrocatalytic hydrogen evolution, *Sci. Adv.* 6 (2020) eaba6586.
- [25] X.L. Jiang, H. Jiang, S.G. Liu, Z.J. Li, M.G. Kim, C. Li, Qing Qin, X.E. Liu, J. Cho, Heterostructure of Ru₂P/WO₃/NPC Synergistically Promotes H₂O Dissociation for Improved Hydrogen Evolution, *Angew. Chem. Int. Ed.* 60 (2021) 4110–4116.
- [26] P. Wang, B.J. Xi, Z.C. Zhang, M. Huang, J.K. Feng, S.L. Xiong, Atomic tungsten on graphene with unique coordination enabling kinetically boosted lithium-sulfur batteries, *Angew. Chem. Int. Ed.* 60 (2021) 15563–15571.
- [27] B.-Y. Guo, X.-Y. Zhang, J.-Y. Xie, Y.-H. Shan, R.-Y. Fan, W.-L. Yu, M.-X. Li, D.-P. Liu, Y.-M. Chai, B. Dong, Ultrafine RuP₂ nanoparticles supported on nitrogen-doped carbon based on coordination effect for efficient hydrogen evolution, *Int. J. Hydrog. Energy* 46 (2021) 7964–7973.
- [28] J.R. Yang, W.-H. Li, S.D. Tan, K.N. Xu, Y. Wang, D.S. Wang, Y.D. Li, The electronic metal-support interaction directing the design of single atomic site catalysts: achieving high efficiency towards hydrogen evolution, *Angew. Chem. Int. Ed.* 60 (2021) 19085–19091.
- [29] H. Li, C. Tsai, A.L. Koh, L.L. Cai, A.W. Contryman, A.H. Fragapane, J.H. Zhao, H. S. Han, H.C. Manoharan, F. Abild-Pedersen, J.K. Nørskov, W.L. Zheng, Activating and optimizing MoS₂ basal planes for hydrogen evolution through the formation of strained sulphur vacancies, *Nat. Mater.* 15 (2016) 48–53.
- [30] Z.-Y. Yu, Y. Duan, J.-D. Liu, Y. Chen, X.-K. Liu, W. Liu, T. Ma, Y. Li, X.-S. Zheng, T. Yao, M.-R. Gao, J.-F. Zhu, B.-J. Ye, S.-H. Yu, Unconventional CN vacancies suppress iron-leaching in Prussian blue analogue pre-catalyst for boosted oxygen evolution catalysis, *Nat. Commun.* 10 (2019) 2799.
- [31] Z.S. Hang, L.H. Tan, F.Y. Ju, B. Zhou, S.Y. Ying, Non-isothermal kinetic studies on the thermal decomposition of melamine by thermogravimetric analysis, *J. Anal. Sci.* 3 (2011) 12–16.
- [32] J.Q. Chi, W.K. Gao, J.H. Lin, B. Dong, K.L. Yan, J.F. Qin, B. Liu, Y.M. Chai, C.G. Liu, Hydrogen evolution activity of ruthenium phosphides encapsulated in nitrogen- and phosphorus-codoped hollow carbon nanospheres, *ChemSusChem* 11 (2018) 743–752.
- [33] H.C. Tao, C. Choi, L.-X. Ding, Z. Jiang, Z.S. Han, M.W. Jia, Q. Fan, Y.N. Gao, H. H. Wang, A.W. Robertson, S. Hong, Y. Jung, S.Z. Liu, Z.Y. Sun, Nitrogen fixation by Ru single-atom electrocatalytic reduction, *Chem* 5 (2019) 204–214.
- [34] P. Chen, T.Y. Xiao, Y.H. Qian, S.S. Li, S.H. Yu, A nitrogen-doped graphene/carbon nanotube nanocomposite with synergistically enhanced electrochemical activity, *Adv. Mater.* 25 (2013) 3192–3196.
- [35] S. Li, B.B. Chen, Y. Wang, M.-Y. Ye, P.A. van Aken, C. Cheng, A. Thomas, Oxygen-evolving catalytic atoms on metal carbides, *Nat. Mater.* 20 (2021) 1240–1247.
- [36] J. Mahmood, F. Li, S.-M. Jung, M.S. Okyay, I. Ahmad, S.-J. Kim, N. Park, H. Y. Jeong, J.-B. Baek, An efficient and pH-universal ruthenium-based catalyst for the hydrogen evolution reaction, *Nat. Nanotechnol.* 12 (2017) 441–446.
- [37] D.S. Baek, G.Y. Jung, B. Seo, J.C. Kim, H.-W. Lee, T.J. Shin, H.Y. Jeong, S.K. Kwak, S.H. Joo, Ordered mesoporous metastable α-MoC_{1-x} with enhanced water dissociation capability for boosting alkaline hydrogen evolution activity, *Adv. Funct. Mater.* 29 (2019), 1901217.
- [38] X.K. Wu, Z.C. Wang, D. Zhang, Y.N. Qin, M.H. Wang, Y. Han, T.R. Zhan, B. Yang, S. X. Li, J.P. Lai, L. Wang, Solvent-free microwave synthesis of ultra-small Ru–Mo₂C@CNT with strong metal-support interaction for industrial hydrogen evolution, *Nat. Commun.* 12 (2021) 4018.
- [39] H. Anwer, J.-W. Park, Addressing the OER/HER imbalance by a redox transition-induced two-way electron injection in a bifunctional n-p-n electrode for excellent water splitting, *J. Mater. Chem. A* 8 (2020) 13218–13230.
- [40] J. Durst, A. Siebel, C. Simon, F. Hasché, J. Herranz, H.A. Gasteiger, New insights into the electrochemical hydrogen oxidation and evolution reaction mechanism, *Energy Environ. Sci.* 7 (2014) 2255–2260.
- [41] Y. Zheng, Y. Jiao, Y.H. Zhu, L.H. Li, Y. Han, Y. Chen, M. Jaroniec, S.-Z. Qiao, High electrocatalytic hydrogen evolution activity of an anomalous ruthenium catalyst, *J. Am. Chem. Soc.* 138 (2016) 16174–16181.
- [42] C. Guan, W. Xiao, H.J. Wu, X.M. Liu, W.J. Zang, H. Zhang, J. Ding, Y.P. Feng, S. J. Pennycook, J. Wang, Hollow Mo-doped Co–Ru nanoarrays for efficient overall water splitting, *Nano Energy* 48 (2018) 73–80.
- [43] J.Y. Zhang, H. Wang, Y. Tian, Y. Yan, Q. Xue, T. He, H. Liu, C. Wang, Y. Chen, B. Y. Xia, Anodic hydrazine oxidation assists energy-efficient hydrogen evolution over

- a bifunctional cobalt perselenide nanosheet electrode, *Angew. Chem. Int. Ed.* 57 (2018) 7649–7653.
- [44] B. Hammer, J.K. Nørskov, Theoretical surface science and catalysis-calculations and concepts, *Adv. Catal.* 45 (2000) 71–129.
- [45] Z.Y. Chen, Y. Song, J.Y. Cai, X.S. Zheng, D.D. Han, Y.S. Wu, Y.P. Zang, S.W. Niu, Y. Liu, J.F. Zhu, X.J. Liu, G.M. Wang, Tailoring the *d*-band centers enables Co₄N nanosheets to be highly active for hydrogen evolution catalysis, *Angew. Chem. Int. Ed.* 57 (2018) 5076–5080.